Biomass Conversion and Biorefinery
https://doi.org/10.1007/s13399-023-04168-y

ORIGINAL ARTICLE

Adsorption/photocatalytic and antibacterial insole of chitosan-stabilized tungsten trioxide nanosheets

Ali A. Keshk[1] · Ahmed Abu-Rayyan[2] · Nadia H. Elsayed[1,7] · Menier Al-Anazi[1] · S. Said[3,4] · Nasser A. Alamrani[1] · Rehan M. El-Shabasy[5] · Kamel R. Shoueir[6]

Received: 2 January 2023 / Revised: 24 March 2023 / Accepted: 2 April 2023

Abstract

Water pollution from wastewater is still a major environmental concern today. One of the most harmful pollutants is a dye, which is produced in large quantities by a variety of industries, including textile, paper, petrochemical, and plastics. Herein, in the presence of biopolymer chitosan (Cs), controllable synthesis of chitosan/tungsten oxide (Cs/WO_3) nanosheet was explored by a precipitation method at room temperature (R.T). The physicochemical properties of Cs/WO_3 nanosheet specimens were evaluated using different tools such as XRD, SEM, TEM, EDX, and UV–Vis spectrophotometry. The tunable size for exhibited sheets ranged from 100 to 400 nm and 60 to 200 nm thickness. Under optimal conditions, the photocatalytic decomposition of methylene blue (MB) was investigated via visible light irradiation, and 0.6 g Cs/WO_3 nanosheet proposed complete decomposition of MB within 40 min at neutral pH. Also, the antibacterial effects of the Cs/WO_3 nanosheet against *Escherichia coli* (*E. coli*) and *Staphylococcus aureus* (*S. aureus*) bacteria are examined. The research demonstrates that the green-prepared WO_3 displays outstanding antibacterial activity against bacterial strains and a drop-in bacterial activity after 24 h.

Keywords Green synthesis · Chitosan/tungsten oxide nanosheets · Photocatalytic · Antibacterial

1 Introduction

Due to their persistent nature and complicated structure, organic dyes generated by the textile industry are considered challenging to decompose. Methylene blue (MB) is a central organic molecule primarily used in the textile industry as a coloring agent, bacteriological stain, human therapeutic agent, redox colorimetric agent, antidote, and disinfectant [1–3]. Despite its beneficial uses, MB threatens both people and marine life owing to its toxicity and carcinogenic consequences, including nausea, vomiting, eye irritation, and diarrhea (adversely affecting aquatic biota) [4, 5]. MB discharge into the environment poses aesthetic and toxicological risks. It blocks light and poisons food chains, and even at

✉ Ali A. Keshk
akeshk@ut.edu.sa

✉ Rehan M. El-Shabasy
rehansh1010@yahoo.com

Nadia H. Elsayed
nhussein@ut.edu.sa

Menier Al-Anazi
Mn.alenazi@ut.edu.sa

S. Said
salah.said@ut.edu.sa

Nasser A. Alamrani
nalomrani@ut.edu.sa

[1] Department of Chemistry, Faculty of Science, University of Tabuk, Tabuk 71474, Saudi Arabia

[2] Chemistry Department, Faculty of Arts & Science, Applied Science Private University, P.O. Box 166, Amman 11931, Jordan

[3] Physics Department, Faculty of Science, University of Tabuk, Tabuk 71421, Saudi Arabia

[4] Physics Department, Faculty of Science, Benha University, Benha, Egypt

[5] Department of Chemistry, Faculty of Science, Menoufia University, Shebin El-Kom 32512, Egypt

[6] Institute of Nanoscience & Nanotechnology, Kafrelsheikh University, Kafrelsheikh 33516, Egypt

[7] Department of Polymers and Pigments, National Research Centre, Giza, Dokki 12311, Egypt

Published online: 01 May 2023

low concentrations, MB in water produces brightly colored subproducts. Due to its high molar absorption coefficient ($\sim 8.4 \times 104$ L mol^{-1} cm^{-1}), MB limits sunlight transmittance, oxygen solubility, aquatic life photosynthetic activity, and biological community variety and aesthetics [5]. As a result, MB dye is a hotly debated subject that requires careful handling before being released into the aquatic ecology [5]. Various water treatment procedures include adsorption, chemical oxidation, photocatalytic degradation, electrochemical degradation, and heterogeneous catalysis were implemented and evaluated before [6, 7].

In contrast to the traditional physical method, such as adsorption, which has demonstrated exemplary performance in removing dye from wastewater, the adsorption technique necessitates a time-consuming process of adsorbent regeneration. Most methods mentioned are frequently expensive, ineffective, time-consuming, and non-destructive to organic pollutants [8]. As a result, it has been discovered that photodegradation is an effective mechanism for dispersing dangerous organic contaminants into non-toxic molecules when exposed to irradiated light [9–11].

The most favorable aspect of a photocatalysis experiment is the photocatalysts, which are both economically advantageous and potentially reused [12]. The photodegradation technique could mainly involve a variety of metal or metal oxides like Pd, TiO_2, and WO_3-doped TiO_2 that is used as a catalyst [13–15]. The majority of earlier studies suggested that the broadband gap of some metal oxides could be a suitable choice for the decomposition of organic contaminants under visible light, but in practice, the narrow band gap is preferable [16, 17]. WO_3 has a small band gap ranging from 2.4 to 2.8 eV in the visible region, so it is used as a significant photocatalyst in addition to its strong stability and nontoxicity [18, 19].

Multiple nanostructures of WO_3 were discussed in the literature to prepare a hierarchical flower [20], nanorods [21], and nanowires [22] using hydrothermal techniques. However, this technique lacks crystallinity, consuming time and energy. Recently, Aliasghari et al. reported the synthesis of wideband gap WO and WO_3. H_2O was estimated by more than 2.6 eV through a novel solution combustion synthesis method; however, the photocatalytic activity was evaluated by 50% [19]. Also, ultrathin WO_3 was synthesized via two steps: first, tungstic acid was distributed in heptanes and dodecyl amine and stirred for 2 days at ambient temperature to generate tungstate-based inorganic organic nanohybrids. Then, the nanohybrids were dispersed in nitric acid, stirred for another 2 days at 10 °C, and ultrasonicated in ice water for 6 h [23].

The performance of WO_3 as an appropriate photocatalyst is constrained by its low photonic efficiency, the rapid recombination rate of the charge carriers (photogenerated hole-electron), and low absorption ranges [24, 25]. High selectivity, fast adsorption rates, and a large adsorption capacity are the essential attributes that set an excellent adsorbent apart from others. In this regard, doping WO_3 with other substances or coated with polymer to increase its photocatalytic activity is thought to be a successful strategy [26–28]. This could enhance the shape of the WO_3 material as well as the band levels and charge carrier properties that are impacted [29]. So, in the present article, a one-step solution based on a green and sustainable approach based on chitosan (Cs) was used to control the synthesis of WO_3 under a simple precipitation process.

Chitosan, a plentiful natural biodegradable polymer, is created through the deacetylation of chitin [11, 30, 31]. This linear polysaccharide is a surface-coating polymer for particles in many medical applications [32, 33]. Coating NPs with Cs has been demonstrated to have numerous benefits in several in vitro and in vivo investigations owing to its nontoxic, biocompatibility, low-cost, FDA-approved, biological activity, and water solubility. These advantages are just a few reasons why Cs is an excellent stabilizer for different metal oxide nanoparticles [34, 35]. Cs also have high effectiveness in water treatment and killing common bacterial species and fungi. Since Cs is a functional polymer, combining it with WO_3 nanoparticles might boost its photocatalytic and antibacterial activities. Because of its outstanding characteristics, Cs is the best polymer for coating WO_3.

Here, a novel green synthesis of lamellar hydrated WO_3 nanosheets was employed using Cs to control phase and size. The photocatalytic degradation of MB over WO_3 and their antibacterial potency were demonstrated.

2 Experimental work

2.1 Chemicals

Tungstic acid sodium salt dihydrate ($Na_2WO_4 \cdot 2H_2O$), oxalic acid ($C_2H_2O_4$), chitosan ($C_{56}H_{103}N_9O_{39}$), acetic acid (CH_3COOH), and potassium dichromate ($K_2Cr_2O_7$) were provided from PubChem. Hydrochloric acid (HCl, ~35% v/v) and absolute ethanol (C_2H_5OH) are supported by Sigma-Aldrich. All of these reagents were employed in analytical grade as it is.

2.2 Green synthesis of Cs/WO_3 nanosheets

A precipitation method was used to synthesize Cs/WO_3 nanosheets at R.T. The synthetic process was displayed by dissolving 1 wt.% of Cs in diluted 50 mL acetic acid and 0.675 g of $Na_2WO_4 \cdot 2H_2O$ (0.15 M) was gradually added to Cs solution to produce a faint yellow color. The reaction lasted 1 h with moderate stirring; the prepared solution was removed by centrifuging. Distilled water and ethanol were

used for repeated washing and then dried in an oven overnight at 70 °C.

2.3 Cs/WO_3 nanostructure characteristics

The surface topography was evaluated using scanning electron microscopy (SEM) and detecting the EDX (S-3400 N II, Hitachi, Japan). A Bruker D2 Phaser X-ray powder diffractometer (30 kV, 10 mA) was employed to analyze the XRD and the Cu anode ($k = 0.15306$ nm). Also, Transmission electron microscopy (TEM) micrograph was used for the detailed morphology of the obtained nanostructure using (A JEOL JEM-2100, Japan). UV–Vis spectra (Shimadzu UV-1208 model) was used for recording the absorption towards photocatalytic application at 25 °C. The surface area of the formed nanoparticles was studied at 77.3 °C using N_2 sorption at 77 K by (Brunauer–Emmett–Teller (BET) surface analyzer (11–2370) Gemini, Micrometrics, USA).

2.4 Photocatalytic depletion of MB over Cs/WO_3 nanosheets

The photocatalytic depletion of MB was investigated through visible light irradiation. The photocatalytic performance was evaluated using 30 mg of the Cs/WO_3 distributed in 40 mL of diluted aqueous solution of MB (15 mg/L) at a neutral pH medium. Afterward, the mixture was sonicated in the dark for 1 h to adjust adsorption and desorption completely (equilibrium) and subjected to a 300-W equivalent halogen lamp (4644 lumens). A UV–Vis absorption spectrophotometer estimated MB concentration as a proportion of irradiation time (Jasco V-530).

2.5 Antibacterial potency

The zone of inhibition (ZOI) method was used to investigate the antibacterial efficiency of Cs/WO_3 nanosheets against both G-negative (*Escherichia coli*) and G-positive (*Staphylococcus aureus*) bacteria under visible light. The nutrient agar culture growth medium is appropriate for this experiment. We estimate the quantity of culture medium needed based on the plate number. Then, pour this amount into the flask, measure the required amount of pure water, and pour it based on the specifications on the container, including the nutrient agar. The solution boiled, and the flask is sealed with cotton and autoclave glue before being placed in the autoclave. We wait for the flask to cool after performing the autoclave and removing it. After that, the agar cool and poured into the plates. Finally, the plates were kept in the incubator for 24 h to ensure they were sterilized. The needle is then burned, and bacteria from the main strain are transferred to cover the surface of the culture medium, followed by the Cs/WO_3 nanosheets to estimate their antibacterial potency. The plates were then placed in an incubator for 24 h to allow the bacteria to grow before measuring the diameter of the ZOI compared to the disk control antibiotic.

3 Results and discussion

3.1 XRD pattern

XRD analysis investigated the as-synthesized nanoparticles' crystalline structural properties and purity. The XRD pattern revealed the major peaks at 2θ values of 21.1, 22.3, 23.5, 25.8, 27.2, 33.7, 34.8, 40.7, 49.1, and 55.3 corresponding to (002), (020), (200), (120), (112), (022), (202), (222), (400), and (420) planes as illustrated in Fig. 1. The XRD analysis supports the monoclinic crystal structure of WO_3 (lattice constants: $a = 7.29$ Å, $b = 7.53$ Å, and $c = 7.68$ Å, JCDPDS: 043–1035). Our results are consistent with previous literature data [36–38]. Additionally, the XRD pattern of the WO_3 revealed sharp peaks, showing a remarkably crystalline feature; the mean size of WO_3 nanoparticles was found to be ~ 255 nm.

3.2 SEM surface texture

The morphological structure of the synthesized sample was investigated by SEM as in Fig. 2. The images show significant homogeneity of the particles with squared

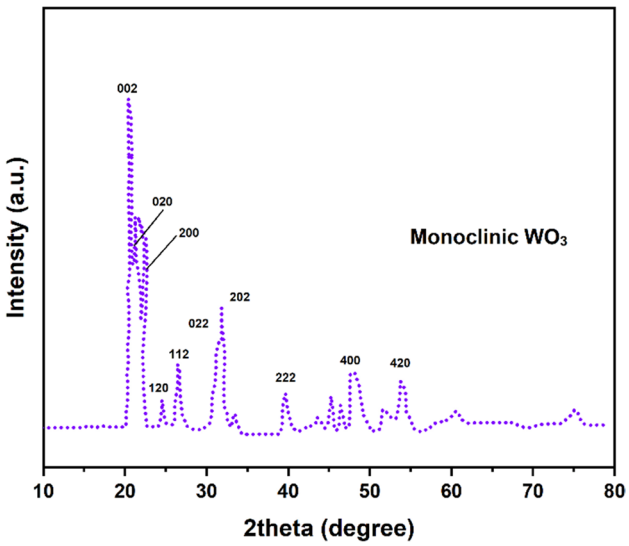

Fig. 1 Powder XRD pattern of monoclinic WO_3

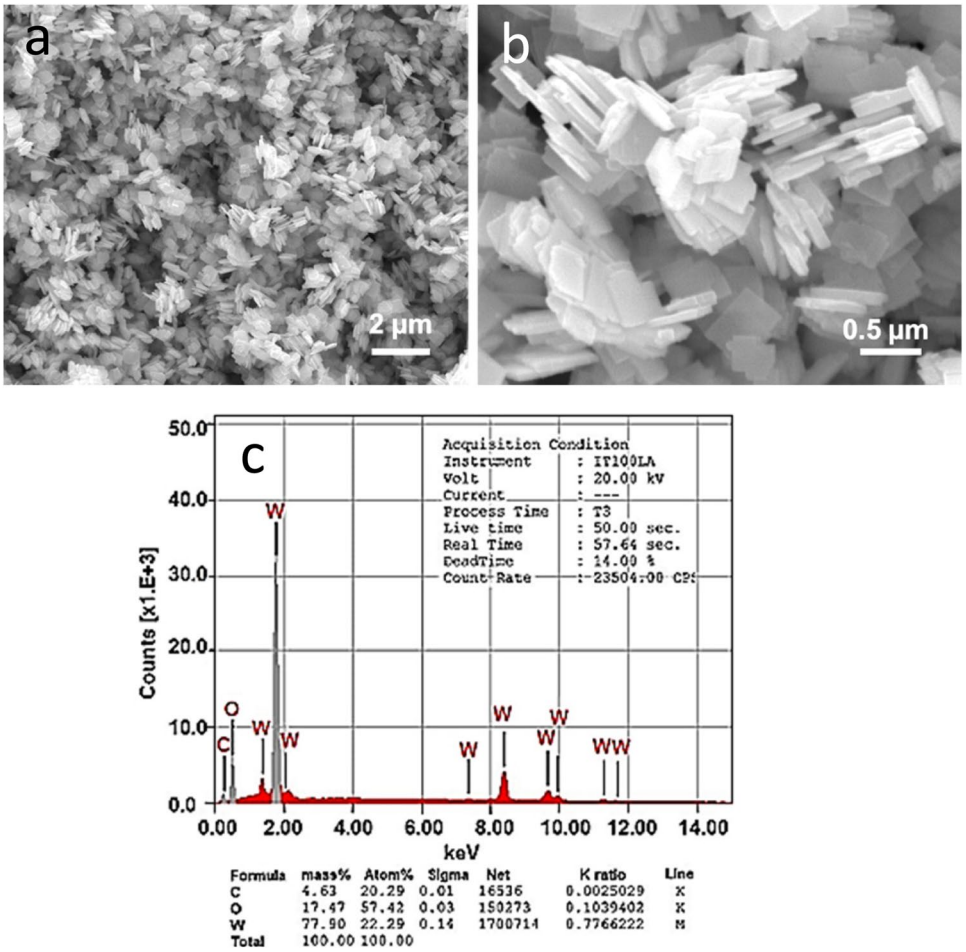

Fig. 2 **a**, **b** FE-SEM image at different scales. **c** Relative EDX spectra

shape, solidified, and some porous appeared. However, the producing sample showed agglomeration composed of some nanosheet layers [39]. The EDX analysis of the as-prepared WO_3 nanosheets displayed clear signals of O and W. The elementary composition of WO_3 nanosheets indicated that the sample was pure form; however, the carbon signal could be from solvent, whereas its amount is minimal, less than 5%.

3.3 TEM shape and size

As shown in Fig. 3, the TEM investigation depicts the WO_3 nanoparticles in a well-defined form and morphology. As detected from TEM, the mean size was around ~ 255 nm. It was observed that the size of the as-synthesized particles revealed in TEM results was consistent with that gained from XRD. Therefore, the electron microscopy examination approves the creation of WO_3 nanoparticles. TEM image exposes the high crystallinity of cubic WO_3 (Fig. 3b, c). The lattice fringes with the crystal spacing of 365.0, 316.0, and 391.0 nm matched the crystal faces of the cubic WO_3 [40–42]. The entire surface of the nanosheet is displayed as a smooth surface that looks like a fingerprint or zebra, and no boundaries have been noticed, this could be useful in different applications. Because of their measured large surface area (113.5 m^2/g), most of these nanosheets choose to be agglomerated or haphazardly overlapped [43, 44]. The structure of monoclinic WO_3 was identified by well-defined facets using the SAED pattern (Fig. 3d), confirming the sample's crystalline nature, which was determined by its XRD pattern.

3.4 Batch adsorption

Figure 4 shows the UV–Vis spectra of the MB dye suspension in contact with Cs/WO_3 nanosheets with varying Cs/WO_3 concentrations (0.1, 0.3, and 0.6 mg) under dark conditions (adsorption property). A cationic MB often has two prominent absorption bands: one at the shoulder at about ~ 618 nm and the other with a center wavelength of ~ 666 nm. Particularly for (0.6 mg) Cs/WO_3, the intensity of the entire peak changes downward as the contact time increases; the change is more pronounced (45 min).

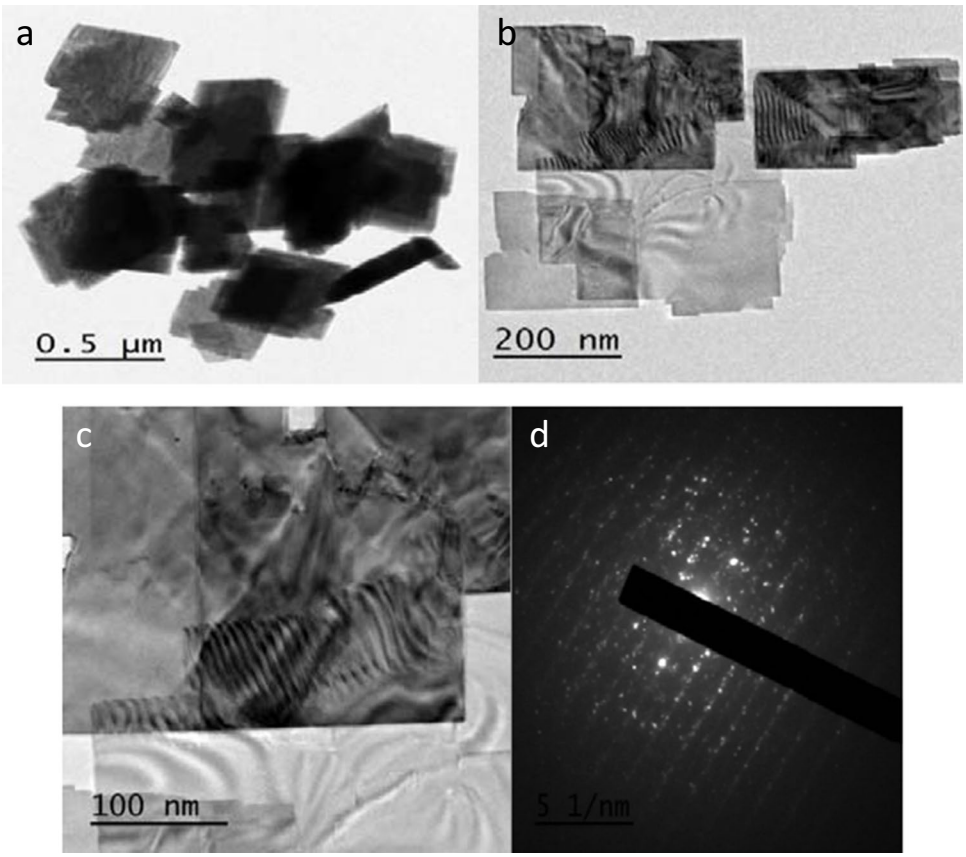

Fig. 3 TEM images of WO_3 nanoparticles at **a** 0.5 µm, **b** 200, and **c** 100 nm with **d** SAED

According to the computed decolorization (%) of MB adsorption for all Cs/WO_3 concentrations, the rates of progressive discoloration for 0.1, 0.3, and 0.6 mg were 51.06% (50 min), 63.62% (60 min), and 85.2 (45 min), respectively. In particular, amidogen in CS and hydroxyl offer open access for MB molecules to enter the interior of Cs/WO_3 and interact with the active sites, boosting the adsorption performance towards MB. Then, the total blocking duration lengthens, and the adsorption intensifies the collision between MB and surface oxidants. Small diffusion controls the removal of MB to interior pores in later stages of adsorption, and consequently, the adsorption process has slowed.

Significant enhancement in average surface qualities (surface area for Cs/WO_3 = 113.5 m^2/g) and the addition of another elementary compositional form, Cs/WO_3, have effectively acted as the active site and have led to improvements. An equation was used to determine adsorption capacity (q_e):

$$q_e(\mathrm{mg/g}) = \frac{(C_0 - C_e)V_1}{M_g} \tag{1}$$

Given that q_e is the quantity of MB that has been adsorbed, C_o is the initial concentration, C_e is the final concentration (mg/L), V is the volume of the pollutant working solution, and M (g) is the contribution of the solid/liquid form of Cs/WO_3 correspondingly. The most common orders to recognize the interaction between the adsorbent and adsorbate are the pseudo-first (PFO)/second-order (PSO) kinetic models [45]. To analyze the adsorption kinetics, PFO and PSO models were used. Below are the empirical calculations [46].

$$\log\left(q_e - q_t\right) = \log q_e - \frac{k_1}{2.303} \tag{2}$$

$$\frac{t}{q_t} = \frac{1}{k_2 q_e^2} + \frac{t}{q_t} \tag{3}$$

q_e and q_t (mg/g) are the adsorbed quantity of MB using Cs/WO_3 at equilibrium and time t, respectively; k_1 is a constant rate of the PFO (min^{-1}), and k_2 is the PSO rate constant ($g.mg^{-1}$) of the adsorption process. To calculate k_2 and R^2, we plotted the ratio of t to q_t and calculated the y-intercept (Fig. 5).

The samples (0.1, 0.3, and 0.6 g) of Cs/WO_3 adsorbent were represented better by PSO. Sample 0.6 g Cs/WO_3 only was figure drawn. All series exhibited higher R^2 = 0.973, 0.941, and 0.996, respectively. At 0.6 g Cs/WO_3, higher

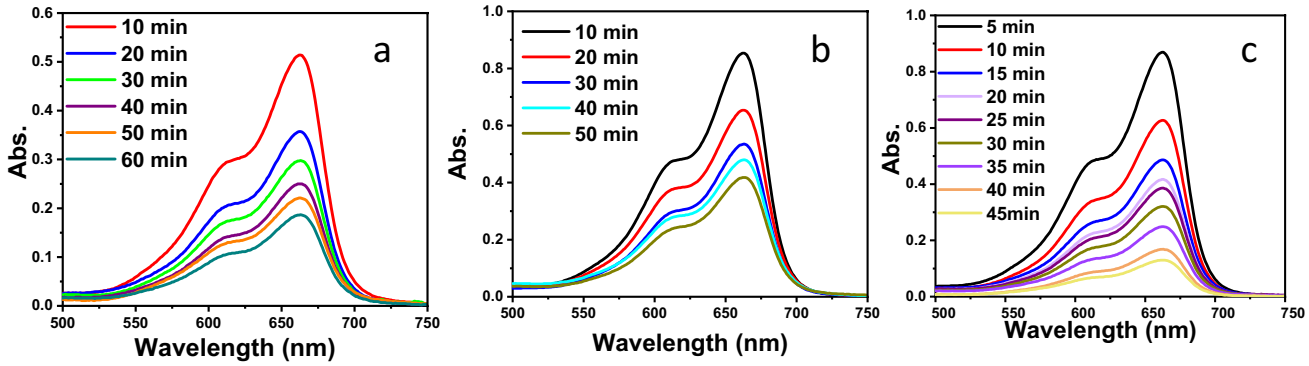

Fig. 4 UV–Vis spectra of the MB period in interaction with **a** 0.1 g Cs/WO_3, **b** 0.3 g Cs/WO_3, and **c** 0.6 g Cs/WO_3

$R^2 = 0.996$, closer to unity. Otherwise, the calculated q maximum agrees well with the calculated q experimental, as shown in Table 1.

Consequently, the presence of a chemical interaction process involving the sharing of electrons between the MB and Cs/WO_3 surface likely regulated the adsorption rate of Cs/WO_3 with varying dosages. Overdose from Cs/WO_3 blocks the active site and consequently hinders the adsorption property, as described in the literature [47]. Furthermore, increasing the catalyst suspension dosage to a specific limit may reduce solution transparency and less efficient radiation penetration [48].

3.5 Photodegradation of MB under visible light

Under visible light and using Cs/WO_3 nanosheets as a nanocatalyst, MB can be broken without any external activator. Figure 6 shows that all Cs/WO_3 contents decomposed MB azo bonds and aromatic rings within maximum 50 min under light irradiation. The absorption band of MB at $\lambda = 667$ nm gradually diminished with the boost illumination. As expected, 0.6 g Cs/WO_3 photocatalyst expanded 100% broken MB. The decomposition efficiency (%) was 85.4, 95.4, and 100% for 0.1, 0.3, and 0.6 g Cs/WO_3, respectively. The findings are explained by promoting the recombination rate

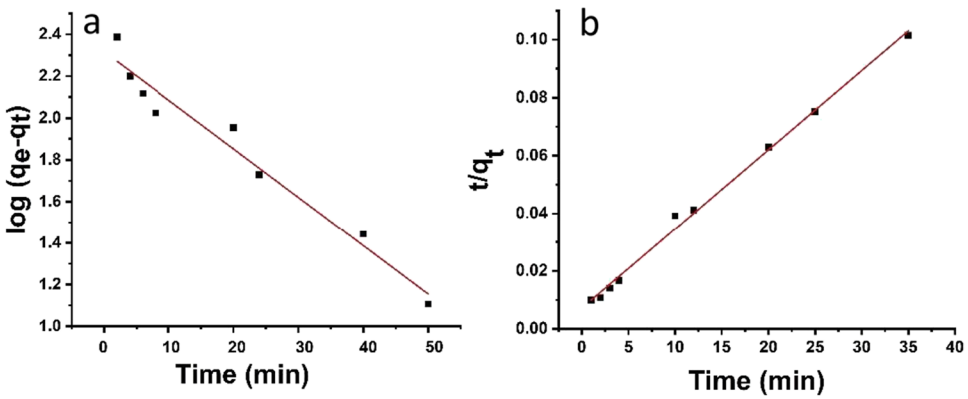

Fig. 5 **A** PFO and **b** PSO for selected 0.6 g Cs/WO_3

Table 1 Kinetics (PFO and PSO) on the dark state for 0.1, 0.3, and 0.6 g Cs/WO_3

Samples	PFO			PSO			
	K_1 (min^{-1})	R_1^2	q_{cal} (mg. g^{-1})	K_2 (gg^{-1} min^{-1}) $\times 10^{-3}$	R_2^2	q_{cal}	q_{exp}
0.1 g Cs/WO_3	0.645	0.881	216.23	4.45	0.973	66.32	68.24
0.3 g Cs/WO_3	0.422	0.899	109.23	3.63	0.941	81.45	83.72
0.6 g Cs/WO_3	0.201	0.912	135.35	2.19	0.996	101.28	104.11

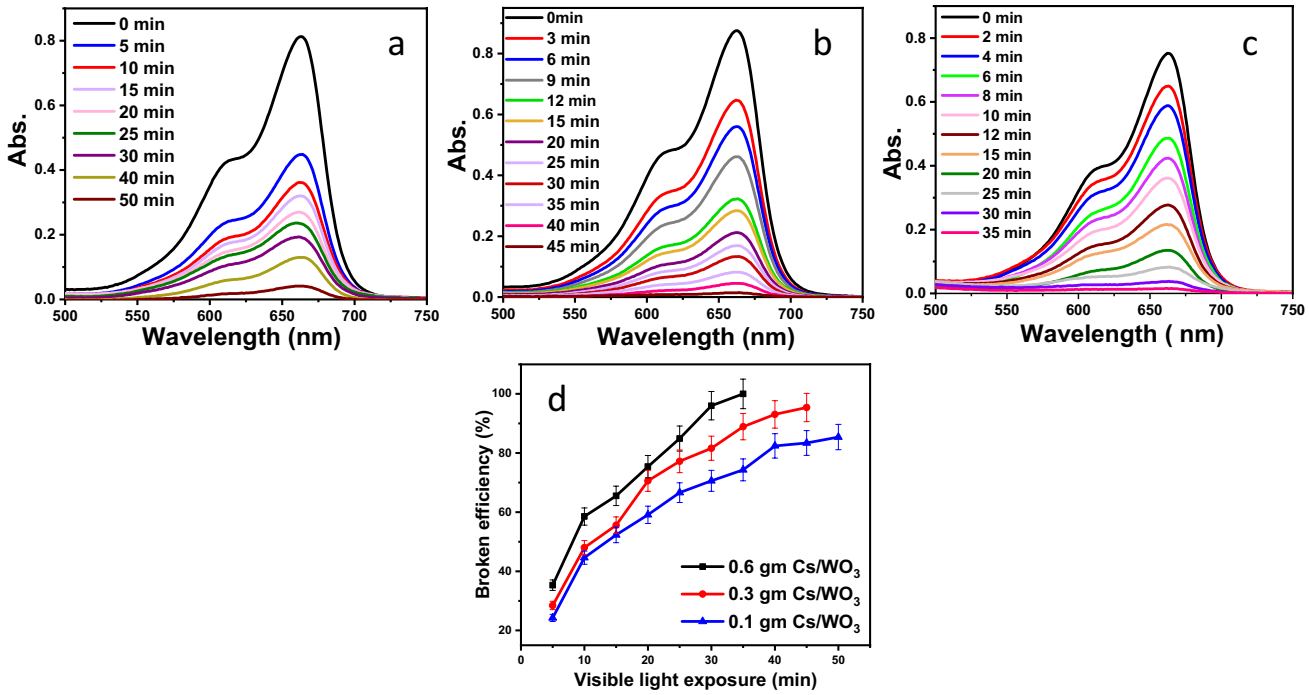

Fig. 6 UV spectrum of MB depletion under solar light for **a** 0.1 g Cs/WO_3, **b** 0.3 g Cs/WO_3, and **c** 0.6 g Cs/WO_3, and **d** breaking efficiency (%)

of charge carriers; in other words, the photogenerated electron–hole is suppressed over 0.6 g Cs/WO_3 photocatalyst, which accepts more absorption of the incident light [31, 49]. A one-way charge transfer (CT) mechanism prevented the recombination of electron–hole pairs; these outcomes are consistent with others [50, 51].

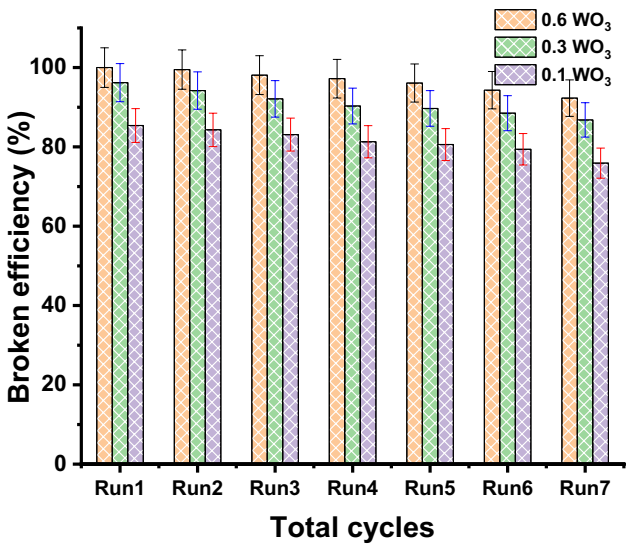

Fig. 7 Recycling performance of different dosages of Cs/WO_3 nanosheets

For mass production, a stable and reusable continuous adsorption method is crucial [52]. The green-prepared Cs/WO_3 was introduced to freshly prepared 15 mg. L^{-1} MB for the following cyclic breakdown test after being withdrawn from the MB solution by centrifugation at 5000 rpm. Figure 7 demonstrates that photodegradation causes a slight decrease in efficiency even after frequent usage. Synergy between the catalytic activity of Cs/WO_3 and Cs functionality led to structural stability, enabling complete degradation of MB [53, 54].

3.6 Mechanism

Cs plays a vital role in the adsorption process of MB through chelation via amino groups along the polymer chain [31]. Additionally, the aromatic ring of the MB molecule interacts negatively with the Cs/WO_3 photocatalyst through π-π interaction, which increases the adsorption of MB and causes dye molecules to bind non-covalently [55]. In Cs/WO_3 photocatalysis, excitation and the photothermal effect promote an electron from the VB to the CB, leaving holes in the VB. This occurs when a beam of light with energy greater than the band gap of Cs/WO_3 is fragmented. This process suppresses the combined photogenerated electrons and holes in the surface of Cs/WO_3. Figure 8 depicts the schematic photodecomposition property of MB over Cs/WO_3 nanosheets. Additionally, a significant amount of photo-excited holes

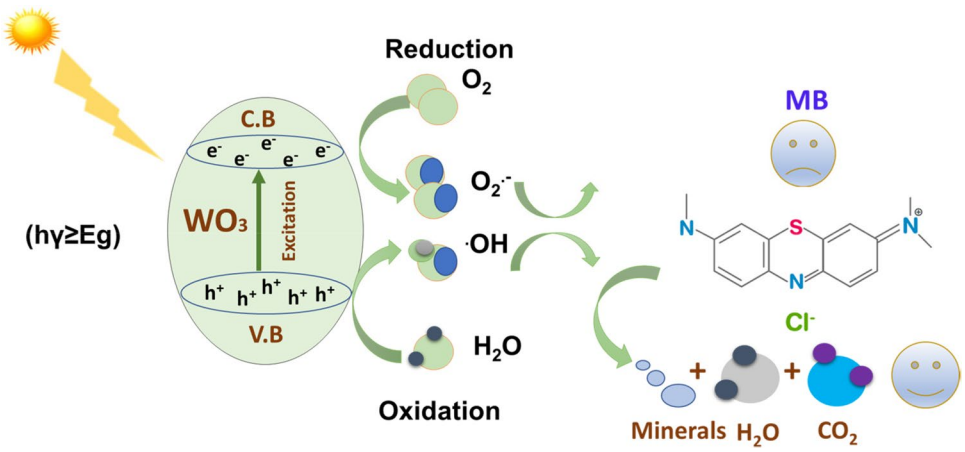

Fig. 8 Schematic photodecomposition property of MB over Cs/WO_3 nanosheets

was preserved, which contributed to the oxidation of MB and improved photocatalytic activity.

More photogenerated holes can react with adsorbed H_2O to produce -OH radicals, accelerating the decomposition of MB. When Cs/WO_3 is protonated, the oxygen adsorbed on its surface accepts electrons to form superoxide radical anions ($O_2^{\cdot-}$), generating -OH. The irradiated light causes these radicals to swoop in and destroy the MB into mineral deposits, carbon dioxide, and water. The photodegradation behavior of MB dyes in the current investigation was compared to that of WO_3 in previously published studies (Table 2).

3.7 Antibacterial potency

Figure 9 depicts that the ZOI by Cs/WO_3 nanosheet against *E. coli* and *S. aureus* was 2.0 ± 0.4 cm and 1.2 ± 0.3 cm.

Table 2 Tungsten oxide (WO_3) and its photodegradation behavior against MB dyes

Catalyst	Shape	Dose	Pollutant	Degradation (%)	Time (min)	Ref
WO_3 sodium alginate/PVP composite	Nanorods (orthorhombic)	3 wt.%	Methylene blue	98%	90	[56]
Aligned WO_3	Nanosheets and nanorods (triclinic, monoclinic and orthorhombic)	0.1 mg/ml	Methylene blue	94%	160	[57]
α-Fe_2O_3/WO_3 composite	WO_3 nanorods and sphere-shaped α-Fe_2O_3 NPs	3 wt.%	Methylene blue	91%	60	[58]
(WO_3-GO)	(Aggregation) monoclinic	15 mg	Methylene blue	97%	180	[59]
Green Cs/WO_3	Nanosheets (monoclinic)	0.6 g	Methylene blue	100%	35	Current study
Green Cs/WO_3	Nanosheets	0.3 g	Methylene blue	95.4%	45	Current study
Green Cs/WO_3	Nanosheets	0.1 g	Methylene blue	85.4%	50	Current study

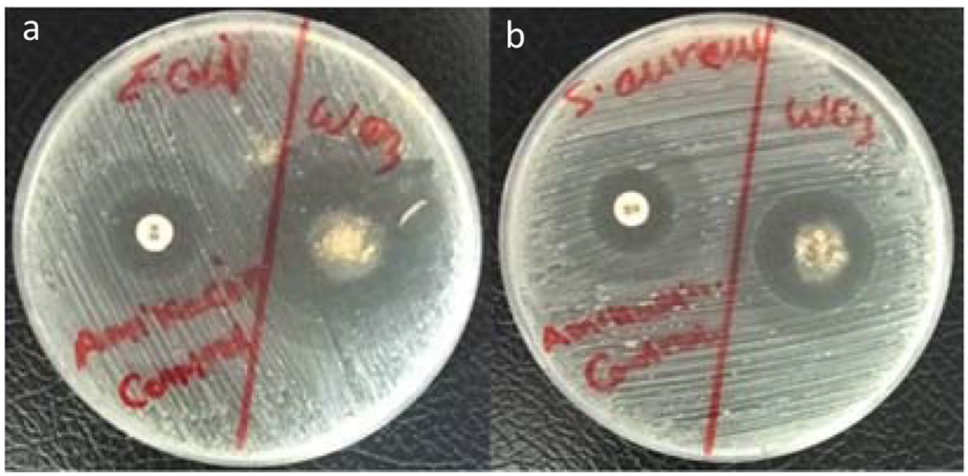

Fig. 9 Antibacterial activity against **a** *E. coli* and **b** *S. aureus* bacterial species

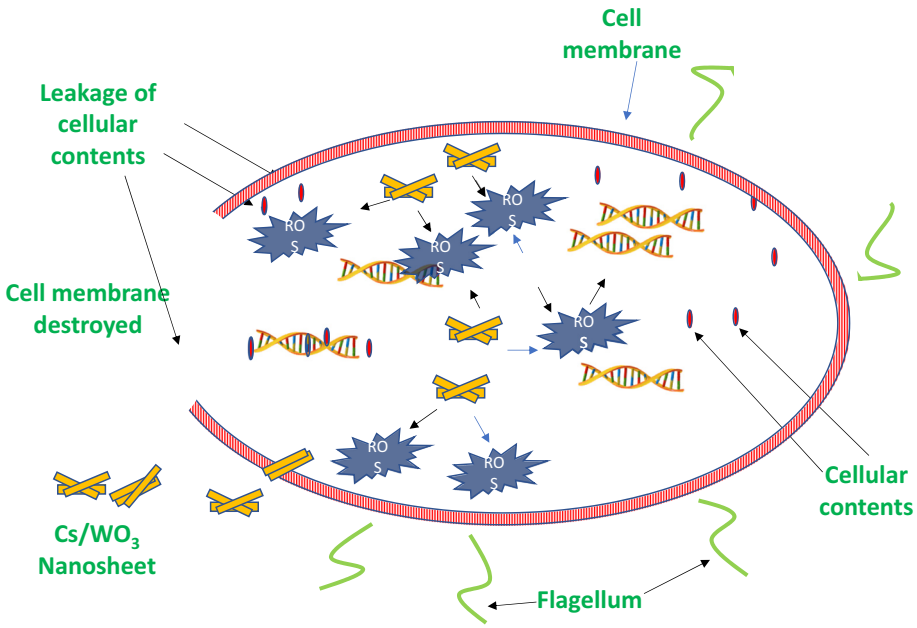

Fig. 10 Suggested antibacterial mechanism of Cs/WO_3

These ZOI diameters were dramatically higher than 0.9 ± 0.1 cm, with amikacin as the control antibiotic. Bacterial cell death is caused by Cs/WO_3 nanosheet through physical destruction and oxidative stress mechanisms.

The direct contact of the Cs/WO_3 nanosheet with the surface of the bacterial cell causes cell membrane integrity to be lost, the liberation of cellular contents, and cell death [60]. With light exposure, Cs/WO_3 nanosheets can generate ROS such as •OH, HO_2•, and H_2O_2. This ROS distortion of the cell wall of bacteria by lipid peroxidation inhibits the growth of bacteria by destroying and inactivating nucleic acids and proteins. Figure 10 depicts this mechanism [61]. This is consistent with the previous study, which used SEM to investigate the antibacterial effect of ultrasmall WO_3 nanodots [62]. According to this study, most *S. aureus* cells collapsed, indicating that their cytoplasm was lost due to direct interaction with the membrane, resulting in a physical disruption. Also, the differences in antibacterial sensitivity between G-positive and G-negative bacterial strains can be attributed to differences in the cell wall and membrane structure. Unlike G-positive bacteria, G-negative bacteria have an outer membrane. By adding another physical layer, an additional membrane may induce G-negative bacteria resistance to the Cs/WO_3 nanosheet [60].

4 Conclusions

As a result, green, one-pot synthesis with chitosan—a traditional precipitation process—was used to create Cs/WO_3, a unique, longitudinally grown photocatalyst. The Cs/WO_3 photocatalyst that has been developed exhibits outstanding MB adsorption and degrading performance at higher dosages (0.6 g Cs/WO_3). The influence of the amino group chitosan structure is primarily responsible for MB fast adsorption and disintegration under light irradiation with the aid of the WO_3 nanosheet. MB totally degraded within 40 min upon using 0.6 g Cs/WO_3. The longitudinally grown materials improved the stability of photocatalytic materials even after seven cycles. According to *E. coli* and *S. aureus*, repetitively, very diluted Cs/WO_3 promotes killing areas that were 2.0 ± 0.4 cm and 1.2 ± 0.3 cm. As a result, this particular transverse, longitudinal structure demonstrated the capacity to digest organic contaminants and bacterial species in polluted water.

Acknowledgements The authors would like to extend their appreciation to the Deanship of Scientific Research at the University of Tabuk for funding this work through research group S-1442-0108.

Author contribution This work has been done by all authors.

Funding The University of Tabuk funded this work through research group S-1442–0108.

Data availability The authors confirm that the data supporting this study are available within the article.

Declarations

Ethical approval Not applicable.

Competing interests The authors declare no competing interests.

References

1. Oladoye PO, Ajiboye TO, EO Omotola, Oyewola OJ (2022) Methylene blue dye: toxicity and potential technologies for elimination from (waste) water. Results in Engineering 16:100678
2. Shoueir K, Kandil S, El-hosainy H, El-Kemary M (2019) Tailoring the surface reactivity of plasmonic Au@ TiO2 photocatalyst bio-based chitosan fiber towards cleaner of harmful water pollutants under visible-light irradiation. J Clean Prod 230:383–393
3. Salama A, Aljohani HA, Shoueir KR (2018) Oxidized cellulose reinforced silica gel: new hybrid for dye adsorption. Mater Lett 230:293–296
4. Xiang X, Zhou J, Lin S, Zhang N, Abulipizi G, Chen G, Li Z (2022) Dual drive acute lethal toxicity of methylene blue to Daphnia magna by polystyrene microplastics and light. Sci Total Environ 840:156681
5. Shoueir K, El-Sheshtawy H, Misbah M, El-hosainy H, El-mehasseb I, El-Kemary M (2018) Fenton-like nanocatalyst for photodegradation of methylene blue under visible light activated by hybrid green DNSA@Chitosan@MnFe2O4. Carbohydr Polym 197:17–28
6. Dihom HR, Al-Shaibani MM, Mohamed RMSR, Al-Gheethi AA, Sharma A, Khamidun MHB (2022) Photocatalytic degradation of disperse azo dyes in textile wastewater using green zinc oxide nanoparticles synthesized in plant extract: a critical review. J Water Process Engineering 47:102705
7. El-Shabasy R, Yosri N, El-Seedi H, Shoueir K, El-Kemary M (2019) A green synthetic approach using chili plant supported Ag/Ag2O@ P25 heterostructure with enhanced photocatalytic properties under solar irradiation. Optik 192:162943
8. Omer AM, Dey R, Eltaweil AS, Abd El-Monaem EM, Ziora ZM (2022) Insights into recent advances of chitosan-based adsorbents for sustainable removal of heavy metals and anions. Arab J Chem 15(2):103543. https://doi.org/10.1016/j.arabjc.2021.103543
9. Jourshabani M, Yun SH, Asrami MR, Lee BK (2022) Superior photodegradation of organic compounds and H2O2 production over tungsten oxide/carbon nitride heterojunction with sizable heptazine units: dual polycondensation and interface engineering. Chem Eng J 427:131710
10. Selvaraj S, Palanivel B, Patrick S, Krishna Mohan M, Navaneethan M, Ponnusamy S, Muthamizhchelvan C (2022) Effect of Sr doping in ZnO microspheres for solar light-driven photodegradation of organic pollutants. J Materials Sci: Materials Electronics 33(11):8777–8788
11. El-Sheshtawy HS, Shoueir KR, El-Kemary M (2020) Activated H2O2 on Ag/SiO2–SrWO4 surface for enhanced dark and visible-light removal of methylene blue and p-nitrophenol. J Alloy Compd 842:155848
12. Shetty K, Prathibha B, Rangappa D, Anantharaju K, Nagaswarupa H, Nagabhushana H, Prashantha S (2017) Photocatalytic study for fabricated Ag doped and undoped MgFe2O4 nanoparticles. Materials Today: Proceedings 4(11):11764–11772
13. Dandapat A, Jana D, De G (2011) Pd nanoparticles supported mesoporous γ-Al2O3 film as a reusable catalyst for reduction of toxic CrVI to CrIII in aqueous solution. Appl Catal A 396(1–2):34–39
14. Yang L, Xiao Y, Liu S, Li Y, Cai Q, Luo S, Zeng G (2010) Photocatalytic reduction of Cr (VI) on WO3 doped long TiO2 nanotube arrays in the presence of citric acid. Appl Catal B 94(1–2):142–149
15. He Z, Cai Q, Wu M, Shi Y, Fang H, Li L, Chen J, Chen J, Song S (2013) Photocatalytic reduction of Cr (VI) in an aqueous suspension of surface-fluorinated anatase TiO2 nanosheets with exposed 001 facets. Ind Eng Chem Res 52(28):9556–9565
16. Nayak AK, Lee S, Choi YI, Yoon HJ, Sohn Y, Pradhan D (2017) Crystal phase and size-controlled synthesis of tungsten trioxide hydrate nanoplates at room temperature: enhanced Cr (VI) photoreduction and methylene blue adsorption properties. ACS Sustain Chem Engineering 5(3):2741–2750
17. Mavinakere Ramesh A, Shivanna S (2018) Visible light assisted photocatalytic degradation of chromium (VI) by using nanoporous Fe2O3. J Mater 1593947:13
18. Buch VR, Chawla AK, Rawal SK (2016) Review on electrochromic property for WO3 thin films using different deposition techniques. Materials Today: Proceedings 3(6):1429–1437
19. Aliasghari H, Arabi A, Haratizadeh H (2020) A novel approach for solution combustion synthesis of tungsten oxide nanoparticles for photocatalytic and electrochromic applications. Ceram Int 46(1):403–414
20. Yang C, Zhu Q, Zhang S, Zou Z, Tian K, Xie C (2014) A comparative study of microstructures on the photoelectric properties of tungsten trioxide films with plate-like arrays. Appl Surf Sci 297:116–124
21. Wang J, Khoo E, Lee PS, Ma J (2008) Synthesis, assembly, and electrochromic properties of uniform crystalline WO3 nanorods. The Journal of Physical Chemistry C 112(37):14306–14312
22. Zhang J, Tu J-P, Xia X-H, Wang X-L, Gu C-D (2011) Hydrothermally synthesized WO 3 nanowire arrays with highly improved electrochromic performance. J Mater Chem 21(14):5492–5498
23. Liang L, Zhang J, Zhou Y, Xie J, Zhang X, Guan M, Pan B, Xie Y (2013) High-performance flexible electrochromic device based on facile semiconductor-to-metal transition realized by WO3· 2H2O ultrathin nanosheets. Sci Rep 3(1):1–8
24. Liu J, Yang L, Li C, Chen Y, Zhang Z (2022) Optimal monolayer WO3 nanosheets/TiO2 heterostructure and its photocatalytic performance under solar light. Chem Phys Lett 804:139861
25. Shandilya P, Sambyal S, Sharma R, Mandyal P, Fang B (2022) Properties, optimized morphologies, and advanced strategies for photocatalytic applications of WO3 based photocatalysts. J Hazard Mater 428:128218
26. Gong F, Yao C, Kong H, Meng E, Gong L, Zhang Y, Li F (2022) WO3/C nanoarchitectures assembled with 1D nanowires: the synthesis, Pt nanoparticles decoration, and highly enhanced hydrogen evolution in neutral media. J Phys Chem Solids 163:110542
27. Munawar T, Mukhtar F, Nadeem MS, Manzoor S, Ashiq MN, Mahmood K, Batool S, Hasan M, Iqbal F (2022) Fabrication of dual Z-scheme TiO2-WO3-CeO2 heterostructured nanocomposite with enhanced photocatalysis, antibacterial, and electrochemical performance. J Alloy Compd 898:162779
28. Moulahoum H, Ghorbanizamani F, Sakarya S, Timur S (2022) Lightless catalytic layered chitosan coating film using doped TiO2@ metal ions nanoparticles for highly efficient dye degradation in aqueous media and disinfection applications. Prog Org Coat 169:106923
29. Kalanur SS, Seo H (2019) Aligned nanotriangles of tantalum doped tungsten oxide for improved photoelectrochemical water splitting. J Alloy Compd 785:1097–1105
30. Asal HA, Shoueir KR, El-Hagrasy MA, Toson EA (2022) Controlled synthesis of in-situ gold nanoparticles onto chitosan functionalized PLGA nanoparticles for oral insulin delivery. Int J Biol Macromol 209:2188–2196
31. Shoueir KR (2020) Green microwave synthesis of functionalized chitosan with robust adsorption capacities for Cr (VI) and/or RHB in complex aqueous solutions. Environ Sci Pollut Res 27(26):33020–33031

32. Trivedi M, Kumar S (2022) Potential of chitosan-based nanocomposites for biomedical application in gene therapy. Springer, Chitosan-Based Nanocomposite Materials, pp 121–144
33. Kou SG, Peters L, Mucalo M (2022) Chitosan: a review of molecular structure, bioactivities and interactions with the human body and micro-organisms. Carbohydr Polym 282:119132
34. Shoueir KR, El-Desouky N, Rashad MM, Ahmed M, Janowska I, El-Kemary M (2021) Chitosan based-nanoparticles and nanocapsules: overview, physicochemical features, applications of a nanofibrous scaffold, and bioprinting. Int J Biol Macromol 167:1176–1197
35. Lyalina T, Lunkov A, Varlamov V (2022) Obtaining of metal nanoparticles using reducing agents and chitosan. Appl Biochem Microbiol 58(2):97–104
36. Kolawole FO, Varela LB, Kolawole SK, Ramirez MA, Tschiptschin AP (2021) Deposition and characterization of tungsten oxide (WO3) nanoparticles incorporated diamond-like carbon coatings using pulsed-DC PECVD. Mater Lett 282:128645
37. Ram J, Singh R, Gupta R, Kumar V, Singh F, Kumar R (2019) Effect of annealing on the surface morphology, optical and and structural properties of nanodimensional tungsten oxide prepared by coprecipitation technique. J Electron Mater 48(2):1174–1183
38. Nayak AK, Verma M, Sohn Y, Deshpande PA, Pradhan D (2017) Highly active tungsten oxide nanoplate electrocatalysts for the hydrogen evolution reaction in acidic and near neutral electrolytes. ACS Omega 2(10):7039–7047
39. Zhang Y, Fu T, Cui K, Shen F, Wang J, Yu L, Mao H (2021) Evolution of surface morphology, roughness and texture of tungsten disilicide coatings on tungsten substrate. Vacuum 191:110297
40. Longobucco G, Pasti L, Molinari A, Marchetti N, Caramori S, Cristino V, Boaretto R, Bignozzi CA (2017) Photoelectrochemical mineralization of emerging contaminants at porous WO3 interfaces. Appl Catal B 204:273–282
41. Si S, Li W, Zhao X, Han M, Yue Y, Wu W, Guo S, Zhang X, Dai Z, Wang X (2017) Significant radiation tolerance and moderate reduction in thermal transport of a tungsten nanofilm by inserting monolayer graphene. Adv Mater 29(3):1604623
42. Zhan T, Tu W, Cheng Y, Han J, Su B, Cheng Y (2018) The synthesis of micro and nano WO3 powders under the sparks of plasma electrolytic oxidation of Al in a tungstate electrolyte. Ceram Int 44(9):10402–10411
43. Yin C, Terentyev D, Zhang T, Nogami S, Antusch S, Chang C-C, Petrov RH, Pardoen T (2021) Ductile to brittle transition temperature of advanced tungsten alloys for nuclear fusion applications deduced by miniaturized three-point bending tests. Int J Refract Metal Hard Mater 95:105464
44. Chang X, Sun S, Zhou Y, Dong L, Yin Y (2011) Solvothermal synthesis of Ce-doped tungsten oxide nanostructures as visible-light-driven photocatalysts. Nanotechnology 22(26):265603
45. Kowanga KD, Gatebe E, Mauti GO, Mauti EM (2016) Kinetic, sorption isotherms, pseudo-first-order model and pseudo-second-order model studies of Cu (II) and Pb (II) using defatted Moringa oleifera seed powder. The J Phytopharmacol 5(2):71–78
46. Bujdák J (2020) Adsorption kinetics models in clay systems. The critical Anal Pseudo-second Order Mechanism, App Clay Sci 191:105630
47. Yin X, Liu L, Ai F (2021) Enhanced photocatalytic degradation of methylene blue by WO3 nanoparticles under NIR light irradiation. Front Chem 9:336
48. Ismail AA, Faisal M, Al-Haddad A (2018) Mesoporous WO3-graphene photocatalyst for photocatalytic degradation of methylene blue dye under visible light illumination. J Environ Sci 66:328–337
49. Shah JH, Fiaz M, Athar M, Ali J, Rubab M, Mehmood R, Jamil SUU, Djellabi R (2019) Facile synthesis of N/B-double-doped Mn2O3 and WO3 nanoparticles for dye degradation under visible light. Environmental Technology 41(18):2372–2381. https://doi.org/10.1080/09593330.2019.1567604
50. Kodarkar N, Deosarkar M, Bhanvase B (2021) Ultrasound assisted one step in-situ preparation and characterization of rGO-WO3 nanocomposite for degradation of organic dyes. Chem Engineering Processing-Process Intensific 163:108367
51. El-Naggar ME, Wassel AR, Shoueir K (2021) Visible-light driven photocatalytic effectiveness for solid-state synthesis of ZnO/natural clay/TiO2 nanoarchitectures towards complete decolorization of methylene blue from aqueous solution. Environ Nanotechnol, Monitoring Management 15:100425
52. Shoueir K, Mohanty A, Janowska I (2022) Industrial molasses waste in the performant synthesis of few-layer graphene and its Au/Ag nanoparticles nanocomposites. Photocatalytic and supercapacitance applications. J Clean Prod 351:131540
53. Entifar SAN, Han JW, Kim JH, Wibowo AF, Park J, Prameswati A, Park SB, Kim M-S, Kim YH (2022) Photocatalytic degradation of methylene blue with carbon coated tungsten trioxide nanoparticles. Opt Mater 133:113032
54. Surakasi R, Rao YS, Sanuj AK, Patil PP, Jayaganthan A, Hechhu R (2022) Methylene Blue dye photodegradation during synthesis and characterization of WO3 nanoparticles. Adsorpt Sci Technol 2882048:10
55. Ghazal S, Mirzaee M, Darroudi M (2022) Green synthesis of tungsten oxide (WO3) nanosheets and investigation of their photocatalytic and cytotoxicity effects. Micro & Nano Letters 17:259–298
56. Elsayed EM, Elnouby MS, Gouda M, Elessawy NA, Santos D (2020) Effect of the morphology of tungsten oxide embedded in sodium alginate/polyvinylpyrrolidone composite beads on the photocatalytic degradation of methylene blue dye solution. Materials 13(8):1905
57. Ahmed B, Kumar S, Ojha AK, Donfack P, Materny A (2017) Facile and controlled synthesis of aligned WO3 nanorods and nanosheets as an efficient photocatalyst material. Spectrochim Acta Part A Mol Biomol Spectrosc 175:250–261
58. Senthil R, Priya A, Theerthagiri J, Selvi A, Nithyadharseni P, Madhavan J (2018) Facile synthesis of α-Fe2O3/WO3 composite with an enhanced photocatalytic and photo-electrochemical performance. Ionics 24(11):3673–3684
59. Jeevitha G, Abhinayaa R, Mangalaraj D, Ponpandian N (2018) Tungsten oxide-graphene oxide (WO3-GO) nanocomposite as an efficient photocatalyst, antibacterial and anticancer agent. J Phys Chem Solids 116:137–147
60. Sharma A, Saini AK, Kumar N, Tejwan N, Singh TA, Thakur VK, Das J (2022) Methods of preparation of metal-doped and hybrid tungsten oxide nanoparticles for anticancer, antibacterial, and biosensing applications. Surfaces and Interfaces 28:101641
61. Wang J, Yang C, Hu X, Yao X, Han L, Wu X, Li R, Wen T, Ming L (2022) Lauric acid induces apoptosis of rice sheath blight disease caused by Rhizoctonia solani by affecting fungal fatty acid metabolism and destroying the dynamic equilibrium of reactive oxygen species. Journal of Fungi 8(2):153
62. Duan G, Chen L, Jing Z, De Luna P, Wen L, Zhang L, Zhao L, Xu J, Li Z, Yang Z (2019) Robust antibacterial activity of tungsten oxide (WO3-X) nanodots. Chem Res Toxicol 32(7):1357–1366